



## Sputtering an exterior metal coating on copper enclosure for large-scale growth of single-crystalline graphene

Paper

Luo, Birong; Caridad, José M; Whelan, Patrick Rebsdorf; Thomsen, Joachim Dahl; Mackenzie, David M A; Grubišić Čabo, Antonija; Mahatha, Sanjoy K.; Bianchi, Marco; Hofmann, Philip; Jepsen, Peter Uhd

*Total number of authors:*

12

*Published in:*

2D materials

*Link to article, DOI:*

[10.1088/2053-1583/aa85d5](https://doi.org/10.1088/2053-1583/aa85d5)

*Publication date:*

2017

*Document Version*

Publisher's PDF, also known as Version of record

[Link back to DTU Orbit](#)

*Citation (APA):*

Luo, B., Caridad, J. M., Whelan, P. R., Thomsen, J. D., Mackenzie, D. M. A., Grubišić Čabo, A., Mahatha, S. K., Bianchi, M., Hofmann, P., Jepsen, P. U., Bøggild, P., & Booth, T. J. (2017). Sputtering an exterior metal coating on copper enclosure for large-scale growth of single-crystalline graphene: Paper. *2D materials*, 4(4), Article 045017. <https://doi.org/10.1088/2053-1583/aa85d5>

---

### General rights

Copyright and moral rights for the publications made accessible in the public portal are retained by the authors and/or other copyright owners and it is a condition of accessing publications that users recognise and abide by the legal requirements associated with these rights.

- Users may download and print one copy of any publication from the public portal for the purpose of private study or research.
- You may not further distribute the material or use it for any profit-making activity or commercial gain
- You may freely distribute the URL identifying the publication in the public portal

If you believe that this document breaches copyright please contact us providing details, and we will remove access to the work immediately and investigate your claim.

PAPER • OPEN ACCESS

## Sputtering an exterior metal coating on copper enclosure for large-scale growth of single-crystalline graphene

To cite this article: Birong Luo *et al* 2017 *2D Mater.* **4** 045017

View the [article online](#) for updates and enhancements.

### Related content

- [Electronic properties and strain sensitivity of CVD-grown graphene with acetylene](#)  
Meng Yang, Shinichirou Sasaki, Masato Ohnishi *et al.*
- [Control of thickness uniformity and grain size in graphene films for transparent conductive electrodes](#)  
Wei Wu, Qingkai Yu, Peng Peng *et al.*
- [Direct growth of graphene on quartz substrates for label-free detection of adenosine triphosphate](#)  
Shicai Xu, Baoyuan Man, Shouzhen Jiang *et al.*

**FlexAL2D<sup>®</sup>**  
ALD for 2D materials

**Nanofab<sup>®</sup>**  
CVD for 2D materials

**OXFORD INSTRUMENTS**  
The Business of Science<sup>®</sup>

[oxinst.com/2DSolutions](http://oxinst.com/2DSolutions)

The advertisement features a blue background with a hexagonal pattern. On the left, the text 'FlexAL2D<sup>®</sup>' is in large orange font, with 'ALD for 2D materials' below it in white. In the center, there is an image of the FlexAL2D machine. On the right, the text 'Nanofab<sup>®</sup>' is in large orange font, with 'CVD for 2D materials' below it in white. In the center, there is an image of the Nanofab machine. At the bottom center, the Oxford Instruments logo is displayed, consisting of the word 'OXFORD' above 'INSTRUMENTS' in white on a dark blue background, with the tagline 'The Business of Science<sup>®</sup>' below it. At the very bottom, the website address 'oxinst.com/2DSolutions' is written in orange.

## OPEN ACCESS

## PAPER



## RECEIVED

15 June 2017

## REVISED

3 August 2017

## ACCEPTED FOR PUBLICATION

11 August 2017

## PUBLISHED

19 September 2017

Original content from this work may be used under the terms of the [Creative Commons Attribution 3.0 licence](https://creativecommons.org/licenses/by/3.0/).

Any further distribution of this work must maintain attribution to the author(s) and the title of the work, journal citation and DOI.



# Sputtering an exterior metal coating on copper enclosure for large-scale growth of single-crystalline graphene

Birong Luo<sup>1</sup>, José M Caridad<sup>1</sup>, Patrick R Whelan<sup>1</sup>, Joachim Dahl Thomsen<sup>1</sup>, David M A Mackenzie<sup>1</sup>, Antonija Grubišić Čabo<sup>2</sup>, Sanjoy K Mahatha<sup>2</sup>, Marco Bianchi<sup>2</sup>, Philip Hofmann<sup>2</sup>, Peter Uhd Jepsen<sup>3</sup>, Peter Bøggild<sup>1</sup> and Timothy J Booth<sup>1</sup>

<sup>1</sup> DTU Nanotech, Technical University of Denmark, Ørsted Plads, 345E, Kgs. Lyngby, 2800, Denmark

<sup>2</sup> Department of Physics and Astronomy, Interdisciplinary Nanoscience Center, Aarhus University, 8000 Aarhus C, Denmark

<sup>3</sup> DTU Fotonik, Technical University of Denmark, Ørsted Plads Building 343, Kgs. Lyngby, 2800, Denmark

E-mail: [tim.booth@nanotech.dtu.dk](mailto:tim.booth@nanotech.dtu.dk)

**Keywords:** graphene, chemical vapor deposition, copper enclosure, sputter, single-crystal

Supplementary material for this article is available [online](#)

## Abstract

We show the suppression of nucleation density in chemical vapor deposited graphene through the use of a sputtered metal coating on the exterior of a copper catalyst enclosure, resulting in the growth of sub-centimeter scale single crystal graphene domains and complete elimination of multilayer growth. The sputtered coating suppresses nucleation density by acting as both a diffusion barrier and as a sink for excess carbon during the growth, reducing the carbon concentration in the interior of the enclosure. Field effect mobility of hBN-templated devices fabricated from graphene domains grown in this way show room temperature carrier mobilities of  $12\,000\text{ cm}^2\text{ V}^{-1}\text{ s}^{-1}$  and an absence of weak localization at low temperature. These results indicate a very low concentration of line and point defects in the grown films, which is further supported by Raman and transmission electron microscopic characterization.

## 1. Introduction

The growth of graphene by metal-catalyzed chemical vapor deposition (CVD) is considered to be the most promising method for synthesis of uniform graphene with a quality approaching that of exfoliated graphene but with the potential for large-scale production [1–3]. To date, single-crystal graphene grains with various morphologies grown by CVD have been achieved and extended growth can knit these separate domains into a continuous film [4]. The resulting polycrystalline film has a grain boundary (line defect) and point defect concentration which is a function of the nucleation density of the individual graphene domains which form it. Both point defects and line defects are undesirable from an applications perspective as they degrade the electronic performance, mechanical strength, thermal conductivity, and oxidation resistance of graphene [5–8]. To reduce grain boundaries, great efforts have been made to either optimize the growth conditions [9–11] or engineer the growth substrates [12–16] for obtaining single-crystalline graphene grains that are as large as possible. The key challenges in growing large single-crystalline graphene grains are to reduce

or passivate nucleation sites on the catalyst surface and to inhibit continuous nucleation during the growth through the supply of the appropriate amount of carbon. To this end, numerous methods, such as increasing temperature [17, 18], extending annealing time [11], diluting methane in Ar [10], high pressure growth [9], vapor trapping [19], repeated growth-etching-regrowth [20], intentional passivation pretreatment [21], and the introduction of O<sub>2</sub> [22–24], have been demonstrated to be effective in reducing nucleation density. The majority of these results have been achieved in hot wall quartz tube systems, which are more difficult to scale up to commercially relevant volumes as compared to cold wall systems. A more serious issue is that the lack of control of the exact position of nucleation sites in these experiments results in randomly positioned graphene domains unless nucleation sites are introduced lithographically [25].

Here, we employ a novel Cu enclosure which integrates either a W or Mo metal coating which acts as a diffusion barrier and excess carbon sink to study the growth of large-scale single-crystalline graphene in a cold wall reactor (Aixtron Black Magic CVD system

shown in supplementary figure S1) ([stacks.iop.org/TDM/4/045017/mmedia](https://stacks.iop.org/TDM/4/045017/mmedia)). The sputtered layer reduces diffusion of carbon through the catalyst bulk and also forms carbides from excess free carbon, which enables the reproducible growth of low nucleation density graphene domains without special changes to the growth recipe and enabling increased yields. We find that the nucleation of graphene domains on the interior of such an enclosure can be completely suppressed under typical growth conditions, and can be controllably raised by a moderate increase of the carbon feedstock supply. Rapid and large-scale growth of millimeter to centimeter scale single-crystalline graphene with high carrier mobility can, therefore, be readily and reproducibly achieved in this way. Moreover, wafer-sized uniform single-layer graphene composed of large grains can be obtained as well. Our study not only demonstrates a facile means of deliberately controlling nucleation density and distribution for obtaining large graphene grains in a cold wall CVD system but also provides insight into the nucleation mechanisms of CVD graphene on low carbon solubility catalysts. This paves the way towards improved crystalline order in CVD graphene films which is critical for the industrialization and commercialization of graphene.

## 2. Results and discussion

It has been shown that the use of an enclosed catalyst ‘pocket’ enables the growth of low nucleation density graphene films on the interior of the enclosure by reducing the rate of carbon precursor flux and reducing the rate of catalyst sublimation [12, 13]. In addition, it has been shown that carbon can diffuse through the bulk copper catalyst layer, affecting the growths on both the interior and exterior surfaces of the catalyst [26]. It is, therefore, natural to ask whether a diffusion barrier can moderate this behavior, and reduce the free carbon concentration in the interior of an enclosure even further. To this end, we sputtered a metal diffusion barrier on the surface of a copper foil and then formed this catalyst foil into an enclosure for the growth of graphene with the sputter coated surface outermost (see figures 1(a)–(c)). Thicknesses of 50–200 nm of both W and Mo were tested and found to operate similarly.

Subsequent CVD growth of graphene on these enclosures show a suppression of nucleation density by around two orders of magnitude, from  $10\text{ mm}^{-2}$  to  $0.1\text{ mm}^{-2}$  as observed in the interior of enclosures partially externally coated in a W diffusion barrier (figures 1(d)–(f)). The average domain size also decreased markedly in the case of barrier-protected catalyst surfaces, from  $150\text{ }\mu\text{m}$  to  $30\text{ }\mu\text{m}$ , indicating much lower carbon availability in these regions. Growths shown here were performed at  $1000\text{ }^\circ\text{C}$  under  $0.1\text{ sccm CH}_4$ ,  $1000\text{ sccm Ar}$  and  $20\text{ sccm H}_2$ , for 1 h (figure S2). Extended growth times of 3 h under increased  $\text{CH}_4$  flow rate of  $0.5\text{ sccm}$  results in complete

coverage on the high nucleation density unprotected interior surfaces, while well separated individual graphene domains are still observed on the interior surface which is protected on the exterior by the diffusion barrier. Additionally, the growth of bilayer regions in the interior of the foil enclosure is completely suppressed. The diffusion barrier acts to block absorption and diffusion of excess carbon species through the catalyst foil and reduce the likelihood of nucleation on the interior surface (figure 1(g)). These results show that the drastic reduction in nucleation density and domain growth rate are a direct result of the exterior barrier coating.

The enclosure is formed by folding and crimping the open edges of the foil, which partially seals the internal gas environment from the outside. This slows the rate of gas exchange with the ambient environment of the CVD chamber and results in a lower availability of carbon for graphene growth on the interior surface. However, in the comparative experiment performed above, the gas environment on the interior of the foil enclosure can be assumed to be uniform, and therefore the resulting difference in the nucleation density must be a result of the exterior barrier metal coating. This barrier metal further reduces the nucleation density below that which might be expected by forming an enclosure alone. The exterior surfaces of the enclosure are exposed to the largest concentration of carbon in the chamber, and growth in this case is rapid with a high nucleation density, and results in complete coverage early in the growth process. Recently, notable improvements in the understanding of growth dynamics and insight into the diffusion mechanisms on the outside and inside surface have been demonstrated, and highlight the importance of diffusion of active carbon species across the thickness of the Cu catalyst layer [26–28]. These species can penetrate the Cu wall which forms the enclosure between interior surface and the exterior surface, which leads to carbon intercalation and growth of the graphene adlayers on the exterior/interior surface. In our case, the W or Mo passivated exterior surface largely reduces the precursor diffusion through the Cu wall to the interior surface of the enclosure from the outside during the initiation of the growth phase. At the exterior surface, this metal coating also acts as an absorbing ‘sink’ to consume the excess carbon species diffused across the Cu wall from inside under a diffusion-driven process formed in such a confined space.

X-ray photoelectron spectroscopy (XPS) highlights a further effect of the exterior coating. After growth, XPS measurements on both the interior and exterior surfaces (figure S4) confirm the presence of carbides in the form of WC seen at  $282.6\text{ eV}$  on the barrier protected exterior surface [29]. The formation of such carbides would additionally reduce the availability of carbon in the interior of the Cu enclosure from the early growth stage, binding the carbon into carbide precipitates [30]. This additional effect further assists

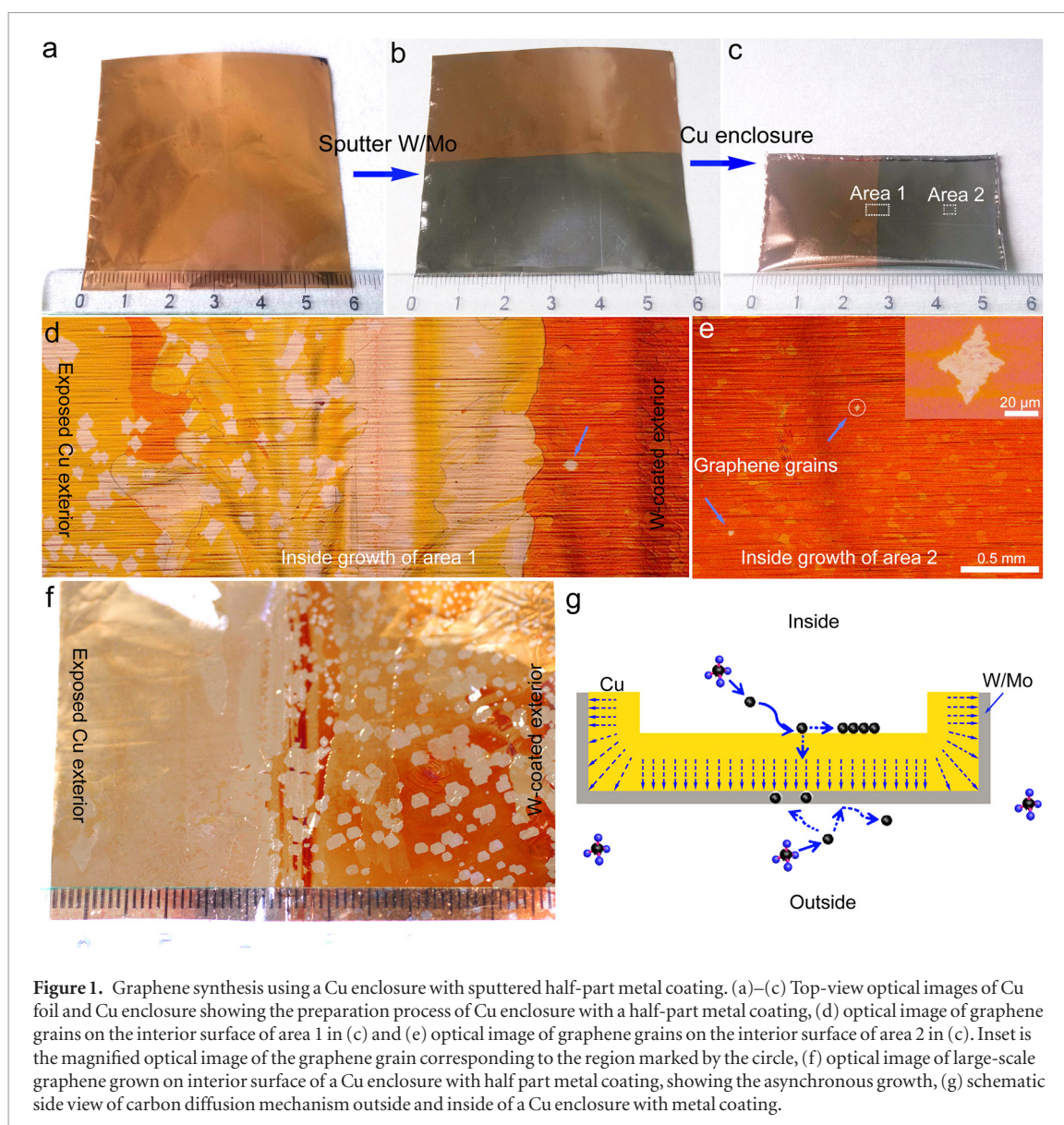


**Figure 1.** Graphene synthesis using a Cu enclosure with sputtered half-part metal coating. (a)–(c) Top-view optical images of Cu foil and Cu enclosure showing the preparation process of Cu enclosure with a half-part metal coating, (d) optical image of graphene grains on the interior surface of area 1 in (c) and (e) optical image of graphene grains on the interior surface of area 2 in (c). Inset is the magnified optical image of the graphene grain corresponding to the region marked by the circle, (f) optical image of large-scale graphene grown on interior surface of a Cu enclosure with half part metal coating, showing the asynchronous growth, (g) schematic side view of carbon diffusion mechanism outside and inside of a Cu enclosure with metal coating.

in maintaining a restricted availability of free carbon in the interior of the enclosure. In contrast, no tungsten carbides were detected at the interior surface by XPS. Trace amounts of W atoms at concentrations below our XPS detection limit might be expected to diffuse through copper foils below the melting temperature, particularly through grain boundary diffusion. If through-diffused traces of W played a role in the suppression of nucleation on the interior, we would expect nucleation to be homogeneously suppressed over the entire foil interior, as surface diffusion is typically an order of magnitude faster than grain boundary diffusion. This is in contrast to our findings, where nucleation is only suppressed where the reverse of the enclosure is coated with W (figures 1(d)–(f)).

To summarize, we propose the following mechanism for the observed graphene growth inside of a Cu enclosure with a reversed metal coating, as illustrated in figure 1(g). Outside the enclosure, the  $\text{CH}_4$  precursor first thermally decomposes to form active carbon species under high temperature. The absorption and

diffusion of these reactive carbon species are inhibited by the sputtered barrier layer, by preventing absorption and sinking excess carbon through the formation of carbides [29, 31].

To further confirm this behavior, we sputtered a complete barrier layer over one side of a copper foil, and formed this foil into an enclosure with the barrier layer outermost (figure 2(a)). The complete diffusion barrier presented by the exterior of this foil results in a total absence of graphene nucleation when an identical CVD growth recipe as that shown in figure 1 is used. This is somewhat surprising given that the enclosure is not expected to be gas tight—it would be reasonable in advance to assume that some nucleation might occur similar to that shown for the partial barrier layers described above. By increasing the  $\text{CH}_4$  flow rate stepwise from 0.2–0.5 sccm and keeping the other parameters unchanged, we are, however, able to not only nucleate graphene on the interior surface, but to controllably alter the domain size by modifying the feedstock flow rate while keeping the duration of

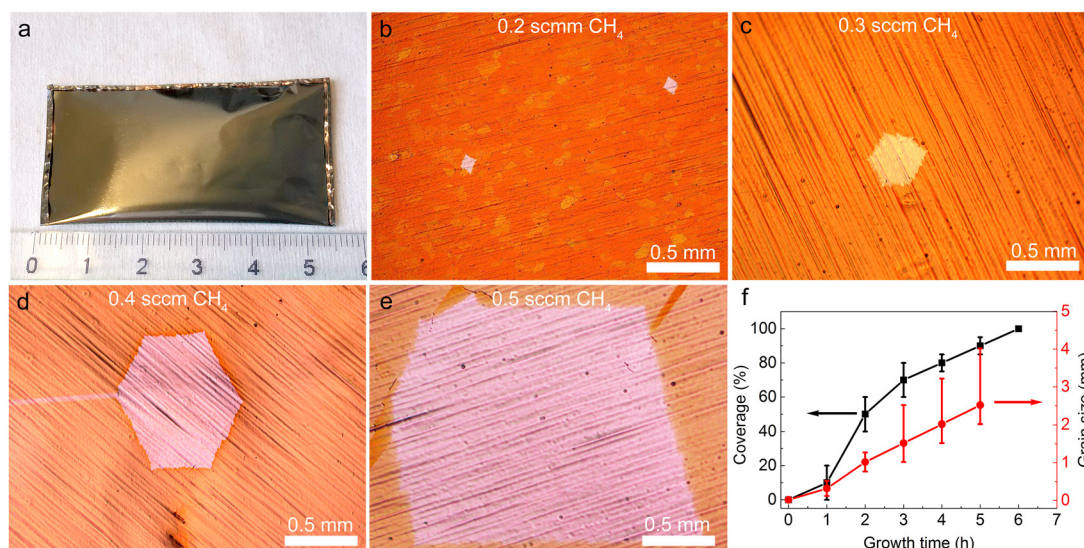


**Figure 2.** Graphene synthesis using a Cu enclosure with full coverage metal coating. (a) Top view optical image of Cu enclosure with sputtered full coverage metal coating, (b)–(e) optical images of graphene grains grown on the interior surface of a Cu enclosure with full coverage metal coating using 1000 sccm Ar, 20 sccm H<sub>2</sub> and varied CH<sub>4</sub> flow rates, (f) the graphene coverage and the average grain size as a function of growth time using 1000 sccm Ar, 20 sccm H<sub>2</sub> and 0.5 sccm CH<sub>4</sub> flow rates.

growth fixed (figures 2(b)–(e)). This identified change in behavior from no nucleation to nucleation is an important condition, as it represents the critical point for the ideal growth of graphene from a single nucleation point. It also confirms that the barrier layer plays a critical role in these growths, by effectively mediating the diffusion and therefore the availability of carbon species in the interior of the enclosure. It is commonly believed that the graphene nucleation process begins with a local supersaturation of active carbon species on the Cu surface, whereupon the nucleation and growth of graphene at active sites on Cu surface is triggered. Based on our observations above, the interior surface of a diffusion barrier protected Cu enclosure shows no graphene nucleation and growth at all using the same growth parameters as in figure 1 (1000 °C under 0.1 sccm CH<sub>4</sub>, 1000 sccm Ar and 20 sccm H<sub>2</sub>), which definitely can produce graphene on common Cu substrates. Again, whilst the interior of the enclosure is sealed to restrict gas exchange it is not expected to be gas tight. This unambiguously indicates that the diffusion of carbon species through the catalyst thickness is critical for nucleation, since the suppression of such diffusion by a metal barrier can completely eliminate nucleation.

As a result of well controlled and disperse nucleation, we are able to grow large domains by changing the CH<sub>4</sub> flow rate from 0.2 to 0.5 sccm resulting in graphene grains approaching the cm scale without individual grains knitting into a complete layer (figures 2(b)–(e)). Tetragonal and hexagonal morphologies can be observed in the grown domains, as determined by the facets of underlying substrates [32] (figure S5(a)). Large single-crystal graphene domains can also grow across Cu grain boundaries (figures S5(b) and (c)), and even the Cu surface irregularities and step bunches (figure S5(d)). In general, extend-

ing the growth time both enlarges the graphene grains and simultaneously increases the graphene coverage. Figure 2(f) shows the graphene coverage and the corresponding grain size grown on the interior of a complete barrier protected Cu enclosure as a function of growth time using 0.5 sccm CH<sub>4</sub> flow rates. As expected, both the graphene coverage and the graphene grain size increases with the growth time varying from 1 to 6 h.

Figure 3(a) shows a typical optical image of large-area single-crystal graphene on the interior surface after 5 h of growth. Isolated graphene grains as large as ~4 mm became optically visible during annealing in air. In addition, the corresponding graphene coverage varies stochastically across the surface as a result of the low nucleation density, but is up to ~90% in some areas. After 6 h of growth, the Cu surface is fully covered by the graphene film—at this point it is not possible to observe the corresponding graphene grains size optically, but is likely to be composed of few mm- to cm-scale graphene grains, with a correspondingly low concentration of grain boundaries. The effect of a lower concentration of grain boundaries on the mechanical properties of the graphene films can be readily seen during transfer to oxidized silicon substrates, where barrier protected films display less cracking and inhomogeneity after transfer than graphene grown with a higher nucleation density (figure 3(b)). Graphene grown on the interior of a barrier-protected enclosure optically shows continuous monolayer graphene. The corresponding unprotected growth region shows a higher optical contrast due to isolated multilayer regions, and a greater non-uniformity due to cracking and tearing during transfer due to the increased number of grain boundaries that result from a higher nucleation density in this region [33]. Terahertz time-domain spectroscopy (THz-TDS) [34, 35] was used to probe the sheet conductivity of the

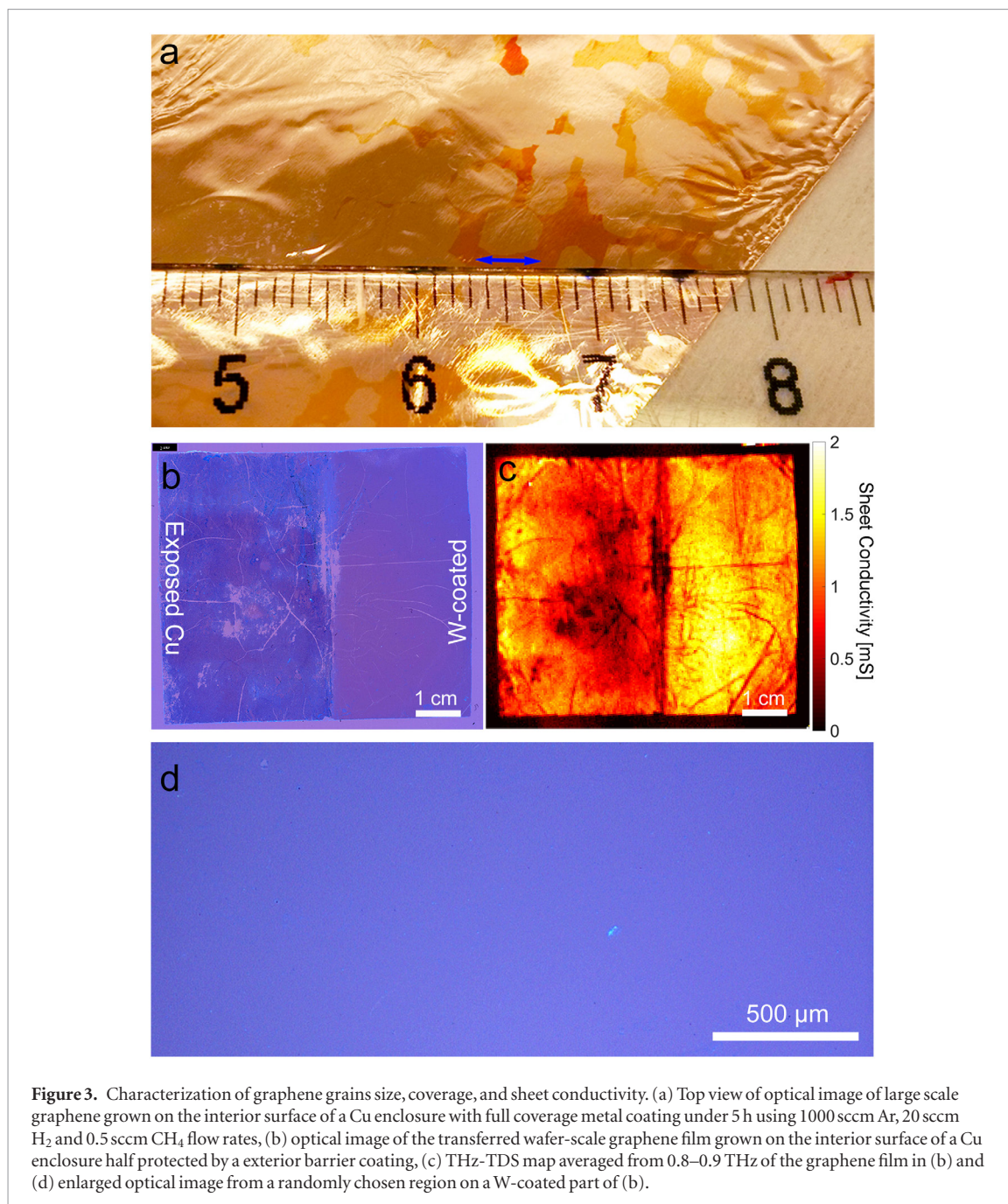


**Figure 3.** Characterization of graphene grains size, coverage, and sheet conductivity. (a) Top view of optical image of large scale graphene grown on the interior surface of a Cu enclosure with full coverage metal coating under 5 h using 1000 sccm Ar, 20 sccm H<sub>2</sub> and 0.5 sccm CH<sub>4</sub> flow rates, (b) optical image of the transferred wafer-scale graphene film grown on the interior surface of a Cu enclosure half protected by an exterior barrier coating, (c) THz-TDS map averaged from 0.8–0.9 THz of the graphene film in (b) and (d) enlarged optical image from a randomly chosen region on a W-coated part of (b).

transferred graphene (figure 3(c)). Graphene from barrier protected regions shows a higher and more homogeneous sheet conductivity than that from unprotected regions, indicating a reduced contribution of grain boundaries, tearing and cracking to the sheet resistance. Graphene transferred to SiO<sub>2</sub>/Si in figure 3(b) displays a uniform monolayer optical contrast (figures 3(d) and S6). The use of a diffusion barrier can, therefore, suppress the formation of graphene multilayers which can occur during graphene growth, even in the case of previously reported enclosure type growths, since there are always excess free active carbon species available at the nucleation sites in the normal Cu enclosure case. The thickness of the barrier layers is sufficient to bind enough carbon in the form of carbides during the growth that a local excess of carbon never occurs and multilayer growths are suppressed.

Raman spectroscopy and transmission electron microscopy (TEM) were conducted to confirm the single-crystal and monolayer nature of the as-grown graphene grains. Figure 4(a) is an optical image of a ~2 mm-sized hexagonal graphene grain transferred onto SiO<sub>2</sub>/Si substrate. Raman spectroscopic mapping (figures 4(b) and S7(a)) shows the  $I_{2D}/I_G$  ratio of peak intensities, with an average of 1.272 (figure S7(b)), verifying its monolayer nature. It is notable that no discernible defect-related D peak was observed (figure S7(a)). Moreover, the  $I_D/I_G$  map (figure 4(c)) shows a highly uniform distribution with negligible  $I_D/I_G$  intensity ratio below 0.02 (figure S7(c)), clearly indicating the low concentration of point defects in the as-grown graphene. A separate ~1.5 mm hexagonal graphene grain was transferred onto a copper TEM grid for TEM investigation. Scanning electron micros-

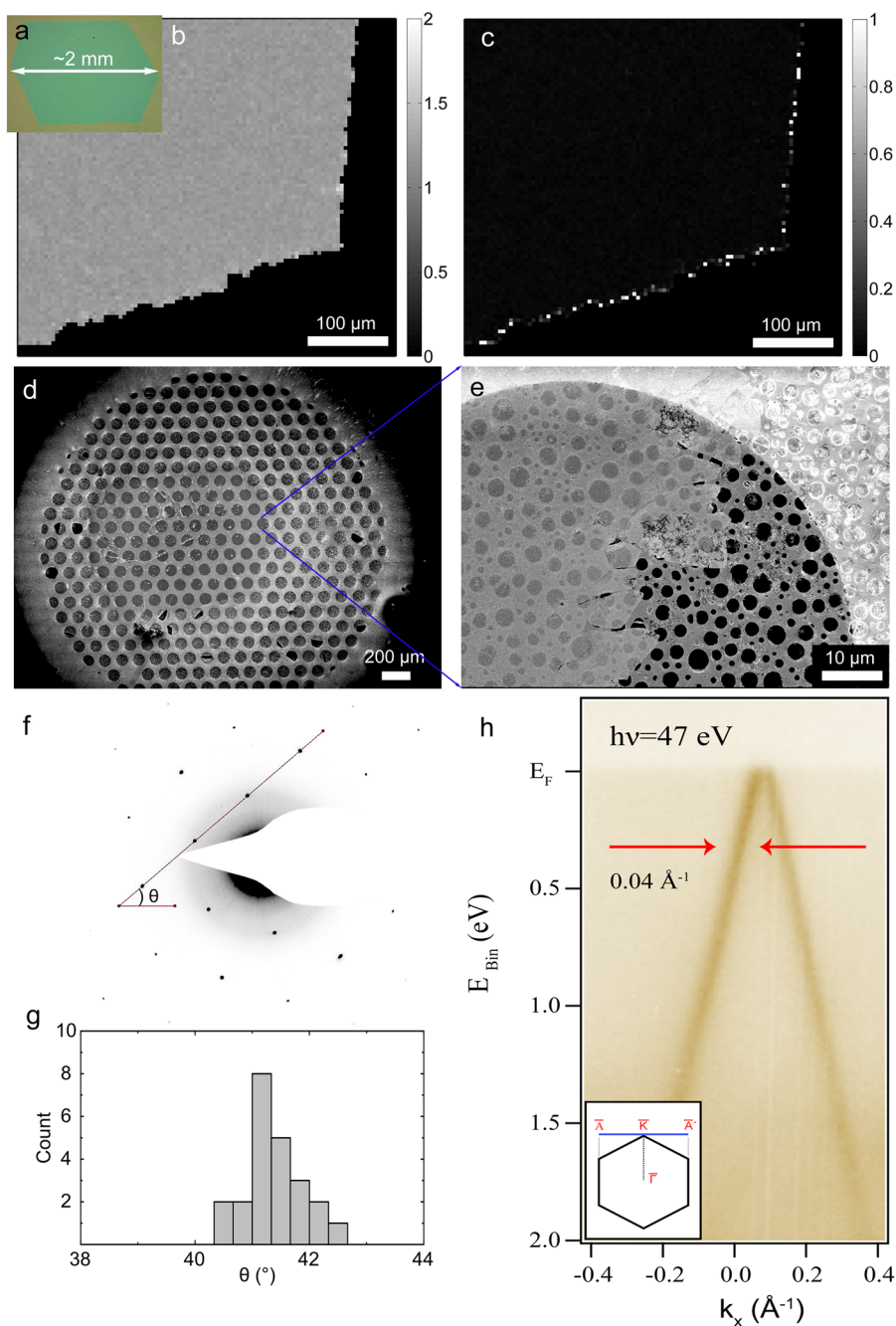
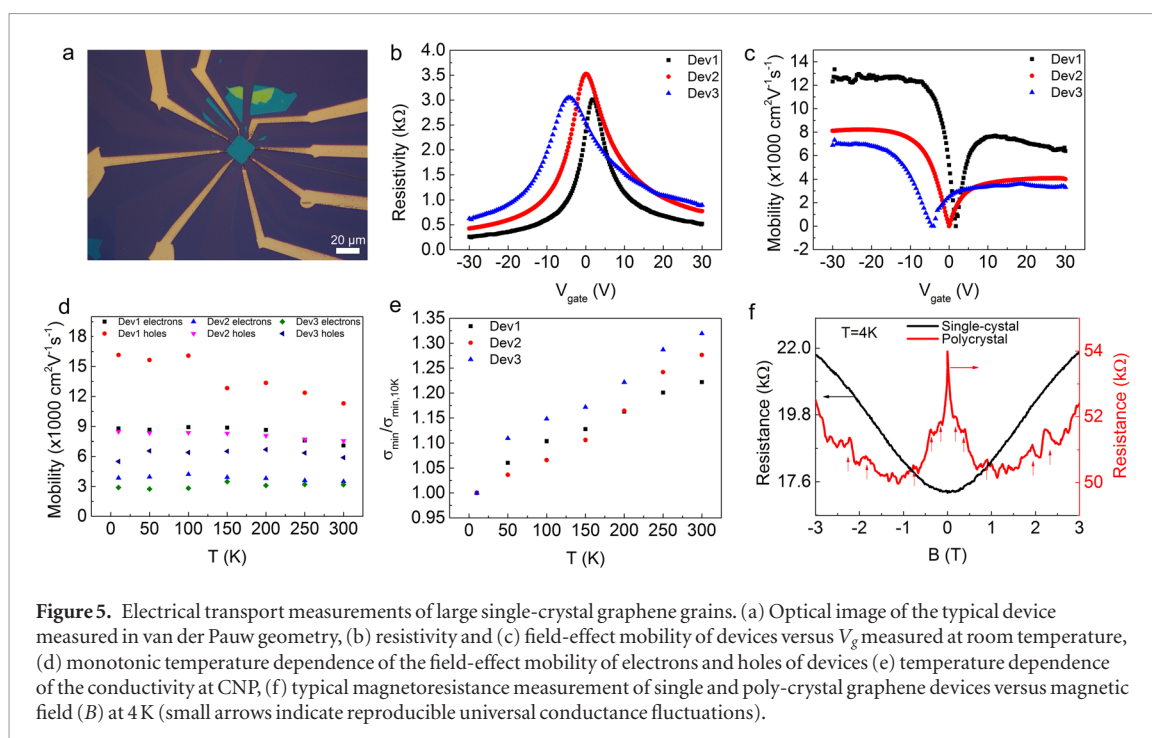


**Figure 4.** Raman, TEM and ARPES characterization of large graphene grains. (a) Optical image of a ~2 mm-size hexagonal graphene grain on SiO<sub>2</sub>/Si, (b) the corresponding  $I_{2D}/I_G$  and (c)  $I_D/I_G$  intensity ratio mapping, (d) SEM image of a ~1.5 mm graphene grain transferred onto a TEM Cu grid, (e) magnified SEM image taken from a hole of the Cu grid, (f) representative SAED patterns taken from (d) and (g) histogram of angle  $\theta$  distribution from multiple SAED patterns obtained from different suspended regions of the same graphene grain, (h) electronic structure of as-grown graphene on copper measured by ARPES, shown as photoemission intensity as a function of binding energy and momentum close to the K point of the Brillouin zone. The scan direction is shown in the inset.

copy (SEM) images of the grid taken after TEM characterization are shown in figures 4(d) and (e). The jagged edge which results from dendritic growth is apparent in the SEM image (figure 4(e)) on holey carbon supported copper grid. Multiple selected area electron diffraction (SAED) patterns were acquired from 23 different regions uniformly distributed across the whole grain to determine the crystalline structure of the graphene. Figures 4(f) and S8 shows typical SAED patterns which show monolayer graphene within each SAED region through a single set of reflections distributed

hexagonally with diffraction spot intensity ratios of  $(1-210)/(1-100) < 1$  (figure S8 inset) and with intensities that are invariant with small tilt angles, confirming its single-layer nature [36, 37]. The indicated relative deviation of the lattice angle  $\theta$  extracted from all of the SAED patterns across the graphene domain shows less than 1° deviation (figure 4(g)), demonstrating that the flake is single-crystal across the entire domain [10], with the single mode in the histogram in figure 4(g) suggesting that variations are not due to small angle grain boundaries, but are more likely to be due to strain.



This observation agrees well with the Raman survey, showing unambiguous single-crystal and monolayer nature of the as-grown graphene grains. Angle resolved photoemission spectroscopy (ARPES) data (figure 4(h)) obtained using a photon energy of 47 eV shows a cross section through the characteristic Dirac cone with the extrapolated Dirac point lying 84 meV above the Fermi level. This slight p-doping of as-grown graphene on Cu is possibly a result of charge transfer from the catalyst layer or from intercalated copper oxides produced by exposure to atmosphere after growth [38]. The line width of the  $\pi$ -band measured 400 meV below the extrapolated Dirac point is  $0.04 \text{ \AA}^{-1}$ , which further indicates the sample is of a high quality [39]. Fermi surface maps are shown in figure S9.

The low concentration of point defects and absence of grain boundaries in the as-grown graphene domains are also reflected in room temperature transport and low-temperature magnetotransport measurements. By wet-transferring a single selected CVD graphene domain on hexagonal boron nitride (hBN), we eliminate the deleterious effects of the substrate from the CVD graphene characterization, focusing more on the influence of grain boundaries and point defects on the electrical transport properties. CVD graphene field effect devices in van der Pauw geometry were fabricated via electron beam lithography (EBL), plasma etching and metal deposition (see experimental section). Figure 5(a) shows the optical top view of a typical graphene field effect device on hBN, where exfoliated hBN flakes on 300 nm  $\text{SiO}_2/\text{Si}$  were prepared in advance, with graphene grains subsequently transferred onto the hBN flakes (figure S10(a)). Supplementary figures S10(b) and (c) illustrate the representative bright and dark field optical image of the area stacked with graphene and hBN, respectively. As shown, the stacked area is

almost free of polymer residues and blisters which usually lead to the deterioration of transport properties [40]. Furthermore, Raman investigation displays the expected hBN and graphene peaks on the stacked area (figure S10(d)), with an increase in the  $I_{2D}/I_G$  ratio to roughly 3 with respect to the case of graphene on  $\text{SiO}_2$  ( $\sim 1.3$ ). We fabricated three such van der Pauw devices, with a  $100 \mu\text{m}^2$  area for each device from different crystals placed on top of a few-layer hBN—we note that the device size here is limited by the availability of sufficiently large exfoliated hBN crystals. These relatively large-area devices are a more robust, convenient and conservative way to evaluate the overall quality of the grown graphene rather than fabricating devices with smaller sizes.

Figure 5(b) shows the room temperature resistivity of the three devices as a function of the gate voltage ( $V_g$ ). They present a small positive and negative shifts of the charge neutrality point (CNP) with respect to 0 V  $V_g$ , indicating largely negligible residual p- or n-doping over the set of devices. The full-width half maximum (FWHM) of the resistivity of our devices is 7 V, 10 V, and 20 V, giving an upper boundary for doping-induced carrier density fluctuations of  $\delta_n < 6 \times 10^{11} \text{ cm}^{-2}$  (Device 1),  $1 \times 10^{12} \text{ cm}^{-2}$  (Device 2) and  $1.5 \times 10^{12} \text{ cm}^{-2}$  (Device 3), respectively. We further extract the room-temperature mobility (calculated in terms of the Drude formula) in our devices, which varies between  $7000\text{--}12\,000 \text{ cm}^2 \text{ V}^{-1} \text{ s}^{-1}$  for holes and  $3000\text{--}7500 \text{ cm}^2 \text{ V}^{-1} \text{ s}^{-1}$  for electrons (figure 5(c)) [41]. These mobility variations and asymmetries in electrons and holes in the measured devices are commonly observed in water assisted, wet-transferred CVD graphene devices. Still, these room temperature mobility values are comparable with those previously achieved from single-crystal, dry-transferred and non-

encapsulated devices on hBN [42]. In addition, devices with higher carrier-density fluctuation  $\delta_n$  (Device 3 > Device 2 > Device 1) show lower carrier mobility (Device 3 < Device 2 < Device 1) (figures 5(b) and (c)), which is consistent with the mobility being limited by Coulomb scattering.

When decreasing the temperature, the mobility of our samples shows a monotonic dependence (figure 5(d)), with a larger effect observed in samples with lower Coulomb scattering. In comparison, this electrical behavior is not present in polycrystalline CVD graphene devices [41, 43], where mobilities show a non-monotonic dependence on temperature regardless of the substrate used. A similar and consistent behavior occurs with conductivity minima  $\sigma_{\min}$  (figure 5(e)). As shown in figure 5(e), the dimensional factor  $\sigma_{\min}/\sigma_{\min,10\text{K}}$  monotonically decreases by a factor of  $\sim 1.3$  between 290 K to 10 K for all our samples, in agreement with the existence of thermally activated transport in these devices for that temperature range [44, 45]. Importantly, this type of transport only appears in graphene devices with low structural disorder [44, 45], indicating the high quality of our single-crystal graphene.

To further confirm that our single-crystal graphene is free of structural defects from a transport viewpoint, we carried out magneto-transport measurements in these devices, and compared these to similar devices produced in the same way but substituting standard polycrystalline CVD graphene for the active region. Figure 5(f) shows a typical magnetoresistance measurement in one of our single-crystal devices close to the CNP under a perpendicular magnetic field ( $B$ ) at 4 K. The overall response of the resistance of the present sample exhibits a positive magnetoresistance (a quadratic dependence on  $B$ ) with no observable signs of weak localization (WL) effects nor universal conductance fluctuations (UCF). This is in stark contrast to the prominent WL effects and reproducible UCF we observe in the polycrystalline graphene device (figure 5(f)), demonstrating both the single-crystallinity of our graphene derived from the presented method (no grain boundaries) and their high structural quality from a transport point of view [5, 46].

### 3. Conclusion

In conclusion, we have demonstrated the suppression of nucleation of CVD graphene in the interior of copper catalyst enclosures through the use of an exterior sputtered barrier layer consisting of W or Mo. This approach enables us to controllably reduce the nucleation density to the point where large few-mm scale single crystal graphene domains of a desired size can be reproducibly grown. The exterior coating provides not only a diffusion barrier, but also a sink for excess carbon species, that can be bound into carbides which are detectable by XPS. Both of these mechanisms help to reduce the concentration of free carbon within the enclosure. We also show that full exterior coverage

of such a barrier layer completely suppresses nucleation of graphene under standard CVD growth conditions, hinting that the nucleation process could be critically dependent on carbon diffusion through the catalyst surface. Low defect density and grain boundary density in barrier protected graphene films from enclosures is demonstrated by Raman spectroscopy, TEM, THz spectroscopy, ARPES and room- and low-temperature magnetotransport measurements, the latter revealing a complete absence of weak localization effects as a result of very low structural disorder. The presented barrier protected catalyst scheme provides multiple advantages for the production of large-scale graphene single crystals by reducing the nucleation density and by suppressing adlayers, establishing a significant step forward in realizing the industrial fabrication of high-quality graphene in a cold wall reactor in an energy-efficient manner.

## 4. Materials and methods

### 4.1. Sputtering W/Mo metal on Cu foil and construction of Cu enclosure

W/Mo with a thickness of 50 nm–200 nm was fully (half) sputtered on the reversed side of Cu foils (25  $\mu\text{m}$  from Alfa Aesar) using a Lesker sputtering system. Before sputtering, the Cu foils were electro-polished to flatten the Cu surface. This was followed by rinses with deionized water and drying under a nitrogen stream. The W/Mo targets were commercially available with a purity of 99.8% wt. The sputtering deposition pressure, power and voltage were maintained at  $\sim 4$  mtorr,  $\sim 150$  W, and  $\sim 350$  V respectively. Cu enclosures were formed by folding and crimping the open edges, sealing the inside Cu environment and displaying the reversed sputtered W/Mo outside (figures 1(a)–(c)).

### 4.2. Graphene synthesis and transfer

Graphene growths were conducted in an Aixtron Black Magic cold wall CVD system (figure S1). After an annealing process in an argon atmosphere, growth is initiated by introducing a methane ( $\text{CH}_4$ ) feedstock in the chamber with varied growth time. The annealing was performed in a mixture of 1000 sccm Ar and 20 sccm  $\text{H}_2$  for 10 min in all cases. Both annealing and growth were performed at low pressure (30 mbar) and under 1000 °C. The as-grown graphene films/grains were transferred onto  $\text{SiO}_2/\text{Si}$  substrates and TEM grids by a poly(methyl methacrylate)-assisted method through etching the copper foils in an aqueous solution. The poly(methyl methacrylate)-supported films were finally removed with acetone.

### 4.3. Characterization of graphene

A Nikon Eclipse L200N microscope equipped with a programmable Prior Scientific XYZ stage and a 5–100 $\times$  objective with NA = 0.3 (0.484  $\mu\text{m}/\text{pixel}$  @ 10 $\times$ ) is used to observe the graphene morphology. Scanning electron microscopy (SEM) (Zeiss Supra VP

60, 10kV) was used to characterize the morphology and location of as-produced graphene. Raman spectroscopy was performed with a Thermo Fisher DXR microscope under ambient conditions using a 455 nm excitation laser source. The nominal spot size is 700 nm. The power of the laser is kept below 1 mW. X-ray photoelectron spectroscopy (XPS) measurements were performed with an Escalab 220i-XL from Thermo Scientific. A monochromatised Al K-Alpha x-ray source with photon energy 1486.7 eV was used as a photon source. TEM (Tecnai G2 F20, operated at 200 kV, with a diameter of  $2\text{ nm}^{-1}$  in the diffraction plane) combined with SAED (with a 200 nm diameter SAED aperture) were used to characterize the crystallinity of as-grown graphene. ARPES measurements were performed at the SGM3 beamline of the synchrotron radiation source ASTRID2 (Aarhus, Denmark) [47]. High-resolution measurements of the  $\pi$ -band were carried out at a temperature of 30 K using a photon energy of 47 eV, with energy and angular resolution better than 20 meV and  $0.2^\circ$ , respectively.

#### 4.4. Device fabrication and electrical transport measurements

hBN-templated graphene field effect devices in van der Pauw geometry were fabricated via EBL, plasma etching, and metal deposition. First, graphene grains were wet-transferred onto 300 nm  $\text{SiO}_2/\text{Si}$  substrates with pre-exfoliated hBN flakes for the stacking. Graphene on hBN areas were identified via optical microscopy and subsequently confirmed by Raman spectroscopy. The EBL was performed in a ZEISS-Leo SEM, with an acceleration voltage of 20 kV. PMMA was used as resist in the EBL process. The etching of the stack is performed in a SPTS ICP Etcher.  $\text{O}_2$  was used to etch the graphene and  $\text{SF}_6$  was used to etch the bottom hBN. We etched hBN in this study in order to more clearly observe the device dimensions under an optical microscope. Metal contacts of Ti (5 nm) and Au (35 nm) were deposited by Physimexa  $\Theta$ FSES250 electron-beam evaporation with low rates. For the electrical transport measurements, resistivity values for van der Pauw devices are measured with Keithley 2400 (sourcemeters) and Keithley 2000 (voltmeters) in a cryostat by applying a constant source-drain bias to two neighboring corner contacts of the device and measuring the voltage drop between the opposite contacts during sweeping of the gate voltage. The sheet resistance  $R_S$  is calculated by applying the reciprocal van der Pauw formula  $\exp(-\pi R_{\text{vertical}}/R_S) + \exp(-\pi R_{\text{horizontal}}/R_S) = 1$ , and the uniformity assessed as described [48].

#### Acknowledgments

This work was supported by the EU Seventh Framework Programme (FP7/2007–2013) under grant agreement number FP7-6040007 ‘GLADIATOR’ and the EC Graphene FET Flagship, grant agreement number

604391, the Danish National Research Foundation Center of Excellence for Nanostructured Graphene (CNG), project DNRF103, VILLUM fonden via the Centre of Excellence for Dirac Materials (Grant No. 11744) and by the Danish Council for Independent Research, Natural Sciences under the Sapere Aude program (Grant No. DFF-4002-00029). P R W and A G C acknowledge financial support from Innovation Fund Denmark DA-GATE 0603-005668B.

#### ORCID iDs

Antonija Grubišić Čabo  <https://orcid.org/0000-0001-7683-0295>

Peter Bøggild  <https://orcid.org/0000-0002-4342-0449>

Timothy J Booth  <https://orcid.org/0000-0002-9784-989X>

#### References

- [1] Alstrup I, Chorkendorff I and Ullmann S 1992 The interaction of  $\text{CH}_4$  at high temperatures with clean and oxygen precovered  $\text{Cu}(100)$  *Surf. Sci.* **264** 95–102
- [2] Li X, Cai W, An J, Kim S, Nah J, Yang D, Piner R, Velamakanni A, Jung I and Tutuc E 2009 Large-area synthesis of high-quality and uniform graphene films on copper foils *Science* **324** 1312–4
- [3] Zhang Y, Zhang L and Zhou C 2013 Review of chemical vapor deposition of graphene and related applications *Acc. Chem. Res.* **46** 2329–39
- [4] Geng D, Wang H and Yu G 2015 Graphene single crystals: size and morphology engineering *Adv. Mater.* **27** 2821–37
- [5] Yu Q, Jauregui L A, Wu W, Colby R, Tian J, Su Z, Cao H, Liu Z, Pandey D and Wei D 2011 Control and characterization of individual grains and grain boundaries in graphene grown by chemical vapour deposition *Nat. Mater.* **10** 443–9
- [6] Vlassioug I, Smirnov S, Ivanov I, Fulvio P F, Dai S, Meyer H, Chi M, Hensley D, Datskos P and Lavrik N V 2011 Electrical and thermal conductivity of low temperature CVD graphene: the effect of disorder *Nanotechnology* **22** 275716
- [7] Huang P Y, Ruiz-Vargas C S, van der Zande A M, Whitney W S, Levendorf M P, Kevek J W, Garg S, Alden J S, Hustedt C J and Zhu Y 2011 Grains and grain boundaries in single-layer graphene atomic patchwork quilts *Nature* **469** 389–92
- [8] Luo B, Whelan P R, Shivayogimath A, Mackenzie D M, Bøggild P and Booth T J 2016 Copper oxidation through nucleation sites of chemical vapor deposited graphene *Chem. Mater.* **28** 3789–95
- [9] Yan Z, Lin J, Peng Z, Sun Z, Zhu Y, Li L, Xiang C, Samuel E L, Kittrell C and Tour J M 2012 Toward the synthesis of wafer-scale single-crystal graphene on copper foils *ACS Nano* **6** 9110–7
- [10] Zhou H, Yu W J, Liu L, Cheng R, Chen Y, Huang X, Liu Y, Wang Y, Huang Y and Duan X 2013 Chemical vapour deposition growth of large single crystals of monolayer and bilayer graphene *Nat. Commun.* **4** 2096
- [11] Wang H, Wang G, Bao P, Yang S, Zhu W, Xie X and Zhang W-J 2012 Controllable synthesis of submillimeter single-crystal monolayer graphene domains on copper foils by suppressing nucleation *J. Am. Chem. Soc.* **134** 3627–30
- [12] Li X, Magnuson C W, Venugopal A, Tromp R M, Hannon J B, Vogel E M, Colombo L and Ruoff R S 2011 Large-area graphene single crystals grown by low-pressure chemical vapor deposition of methane on copper *J. Am. Chem. Soc.* **133** 2816–9

- [13] Chen S, Ji H, Chou H, Li Q, Li H, Suk J W, Piner R, Liao L, Cai W and Ruoff R S 2013 Millimeter-size single-crystal graphene by suppressing evaporative loss of Cu during low pressure chemical vapor deposition *Adv. Mater.* **25** 2062–5
- [14] Lee J-H, Lee E K, Joo W-J, Jang Y, Kim B-S, Lim J Y, Choi S-H, Ahn S J, Ahn J R and Park M-H 2014 Wafer-scale growth of single-crystal monolayer graphene on reusable hydrogen-terminated germanium *Science* **344** 286–9
- [15] Nguyen V L, Shin B G, Duong D L, Kim S T, Perello D, Lim Y J, Yuan Q H, Ding F, Jeong H Y and Shin H S 2015 Seamless stitching of graphene domains on polished copper (1 1 1) foil *Adv. Mater.* **27** 1376–82
- [16] Wu T, Zhang X, Yuan Q, Xue J, Lu G, Liu Z, Wang H, Wang H, Ding F and Yu Q 2016 Fast growth of inch-sized single-crystalline graphene from a controlled single nucleus on Cu–Ni alloys *Nat. Mater.* **15** 43–7
- [17] Li X, Magnuson C W, Venugopal A, An J, Suk J W, Han B, Borysiak M, Cai W, Velamakanni A and Zhu Y 2010 Graphene films with large domain size by a two-step chemical vapor deposition process *Nano Lett.* **10** 4328–34
- [18] Vlasiouk I, Smirnov S, Regmi M, Surwade S P, Srivastava N, Feenstra R, Eres G, Parish C, Lavrik N and Datskos P 2013 Graphene nucleation density on copper: fundamental role of background pressure *J. Phys. Chem. C* **117** 18919–26
- [19] Wang C, Chen W, Han C, Wang G, Tang B, Tang C, Wang Y, Zou W, Zhang X-A and Qin S 2014 Growth of millimeter-size single crystal graphene on Cu foils by circumfluence chemical vapor deposition *Sci. Rep.* **4** 4537
- [20] Ma T, Ren W, Liu Z, Huang L, Ma L-P, Ma X, Zhang Z, Peng L-M and Cheng H-M 2014 Repeated growth-etching-regrowth for large-area defect-free single-crystal graphene by chemical vapor deposition *ACS Nano* **8** 12806–13
- [21] Lin L, Li J, Ren H, Koh A L, Kang N, Peng H, Xu H and Liu Z 2016 Surface engineering of copper foils for growing centimeter-sized single-crystalline graphene *ACS Nano* **10** 2922–9
- [22] Hao Y, Bharathi M, Wang L, Liu Y, Chen H, Nie S, Wang X, Chou H, Tan C and Fallahzad B 2013 The role of surface oxygen in the growth of large single-crystal graphene on copper *Science* **342** 720–3
- [23] Gan L and Luo Z 2013 Turning off hydrogen to realize seeded growth of subcentimeter single-crystal graphene grains on copper *ACS Nano* **7** 9480–8
- [24] Guo W, Jing F, Xiao J, Zhou C, Lin Y and Wang S 2016 Oxidative-etching-assisted synthesis of centimeter-sized single-crystalline graphene *Adv. Mater.* **28** 3152–8
- [25] Wu W, Jauregui L A, Su Z, Liu Z, Bao J, Chen Y P and Yu Q 2011 Growth of single crystal graphene arrays by locally controlling nucleation on polycrystalline Cu using chemical vapor deposition *Adv. Mater.* **23** 4898–903
- [26] Fang W, Hsu A L, Song Y, Birdwell A G, Amani M, Dubey M, Dresselhaus M S, Palacios T and Kong J 2014 Asymmetric growth of bilayer graphene on copper enclosures using low-pressure chemical vapor deposition *ACS Nano* **8** 6491–9
- [27] Zhao Z, Shan Z, Zhang C, Li Q, Tian B, Huang Z, Lin W, Chen X, Ji H and Zhang W 2015 Study on the diffusion mechanism of graphene grown on copper pockets *Small* **11** 1418–22
- [28] Hao Y, Wang L, Liu Y, Chen H, Wang X, Tan C, Nie S, Suk J W, Jiang T and Liang T 2016 Oxygen-activated growth and bandgap tunability of large single-crystal bilayer graphene *Nat. Nanotechnol.* **11** 426–31
- [29] Shin Y C 2015 Application of tungsten as a carbon sink for synthesis of large-domain uniform monolayer graphene free of bilayers/multilayers *Nanoscale* **7** 4929–34
- [30] Chen C-C, Kuo C-J, Liao C-D, Chang C-F, Tseng C-A, Liu C-R and Chen Y-T 2015 Growth of large-area graphene single crystals in confined reaction space with diffusion-driven chemical vapor deposition *Chem. Mater.* **27** 6249–58
- [31] Dai B, Fu L, Zou Z, Wang M, Xu H, Wang S and Liu Z 2011 Rational design of a binary metal alloy for chemical vapour deposition growth of uniform single-layer graphene *Nat. Commun.* **2** 522
- [32] Meca E, Lowengrub J, Kim H, Mattevi C and Shenoy V B 2013 Epitaxial graphene growth and shape dynamics on copper: phase-field modeling and experiments *Nano Lett.* **13** 5692–7
- [33] Kim K, Johnson R W, Tanskanen J T, Liu N, Kim M-G, Pang C, Ahn C, Bent S F and Bao Z 2014 Selective metal deposition at graphene line defects by atomic layer deposition *Nat. Commun.* **5** 4781
- [34] Buron J D, Pizzocchero F, Jessen B S, Booth T J, Nielsen P F, Hansen O, Hilke M, Whiteway E, Jepsen P U and Bøggild P 2014 Electrically continuous graphene from single crystal copper verified by terahertz conductance spectroscopy and micro four-point probe *Nano Lett.* **14** 6348–55
- [35] Buron J D, Mackenzie D M, Petersen D H, Pesquera A, Centeno A, Bøggild P, Zurutuza A and Jepsen P U 2015 Terahertz wafer-scale mobility mapping of graphene on insulating substrates without a gate *Opt. Express* **23** 30721–9
- [36] Meyer J C, Geim A K, Katsnelson M I, Novoselov K S, Booth T J and Roth S 2007 The structure of suspended graphene sheets *Nature* **446** 60–3
- [37] Luo B, Chen B, Wang A, Geng D, Xu J, Wang H, Zhang Z, Peng L, Xu Z and Yu G 2016 Chemical vapor deposition of bilayer graphene with layer-resolved growth through dynamic pressure control *J. Mater. Chem. C* **4** 7464–71
- [38] Larciprete R, Ulstrup S, Lacovig P, Dalmiglio M, Bianchi M, Mazzola F, Hornekaer L, Orlando F, Baraldi A and Hofmann P 2012 Oxygen switching of the epitaxial graphene-metal interaction *ACS Nano* **6** 9551–8
- [39] Pletikosić I, Kralj M, Pervan P, Brako R, Coraux J, N'Diaye A T, Busse C and Michely T 2009 Dirac cones and minigaps for graphene on Ir(1 1 1) *Phys. Rev. Lett.* **102** 056808
- [40] Pizzocchero F, Gammelgaard L, Jessen B S, Caridad J M, Wang L, Hone J, Bøggild P and Booth T J 2016 The hot pick-up technique for batch assembly of van der Waals heterostructures *Nat. Commun.* **7** 11894
- [41] Gannett W, Regan W, Watanabe K, Taniguchi T, Crommie M and Zettl A 2011 Boron nitride substrates for high mobility chemical vapor deposited graphene *Appl. Phys. Lett.* **98** 242105
- [42] Calado V, Zhu S-E, Goswami S, Xu Q, Watanabe K, Taniguchi T, Janssen G and Vandersypen L 2014 Ballistic transport in graphene grown by chemical vapor deposition *Appl. Phys. Lett.* **104** 023103
- [43] Zhong B, Uddin M A, Singh A, Webb R and Koley G 2016 Temperature dependent carrier mobility in graphene: effect of Pd nanoparticle functionalization and hydrogenation *Appl. Phys. Lett.* **108** 093102
- [44] Dean C R, Young A F, Meric I, Lee C, Wang L, Sorgenfrei S, Watanabe K, Taniguchi T, Kim P and Shepard K 2010 Boron nitride substrates for high-quality graphene electronics *Nat. Nanotechnol.* **5** 722–6
- [45] Han M Y, Brant J C and Kim P 2010 Electron transport in disordered graphene nanoribbons *Phys. Rev. Lett.* **104** 056801
- [46] Tikhonenko F, Kozikov A, Savchenko A and Gorbachev R 2009 Transition between electron localization and antilocalization in graphene *Phys. Rev. Lett.* **103** 226801
- [47] Hoffmann S, Søndergaard C, Schultz C, Li Z and Hofmann P 2004 An undulator-based spherical grating monochromator beamline for angle-resolved photoemission spectroscopy *Nucl. Instrum. Methods Phys. Res. A* **523** 441–53
- [48] Mackenzie D M, Buron J D, Whelan P R, Caridad J M, Bjergfelt M, Luo B, Shivayogimath A, Smitshuysen A L, Thomsen J D and Booth T J 2017 Quality assessment of graphene: continuity, uniformity, and accuracy of mobility measurements *Nano Res.* **1**–10